IEEE Access
Multidisciplinary | Rapid Review | Open Access Journal

Received May 22, 2019, accepted May 31, 2019, date of publication June 10, 2019, date of current version June 21, 2019.

Digital Object Identifier 10.1109/ACCESS.2019.2921839

Calculation and Analysis of Constant Stiffness Space for Redundant Cable-Driven Parallel Robots

ZHIWEI CUI[1], XIAOQIANG TANG[1,2,3], SENHAO HOU[1], HAINING SUN[1], AND DIANJUN WANG[4]

[1]Department of Mechanical Engineering, Tsinghua University, Beijing 100084, China
[2]State Key Laboratory of Tribology, Tsinghua University, Beijing 100084, China
[3]Beijing Key Laboratory of Precision/Ultra-Precision Manufacturing Equipment and Control, Tsinghua University, Beijing 100084, China
[4]Mechanical Engineering Academy, Beijing Institute of Petrochemical Technology, Beijing 102617, China

Corresponding author: Xiaoqiang Tang (tang-xq@mail.tsinghua.edu.cn)

This research was supported in part by the National Natural Science Foundation of China under Grant 91648107 and in part by the Beijing Natural Science Foundation under Grant L182041.

ABSTRACT In this paper, a new concept of the constant stiffness space (CSS) of cable-driven parallel robots (CDPRs) is presented to meet the requirement for the constant stiffness plane of CDPRs in ground simulation spacecraft landing addressing experiments. First, the previously studied stiffness model and cable tension feasible region are reviewed. Then, the concept of the stiffness relative contribution coefficient is proposed, which can directly reflect the influence of controllable stiffness on system stiffness and guide the selection of driving cables and the setting of cable tension limiting values. Further, a method to calculate the CSS is proposed. This method can effectively obtain the CSS of robots according to the target stiffness. Next, an evaluation index for the local and global stability of the CSS is presented to analyze and evaluate the stability of the CSS of CDPRs. The influences of the load and posture of the end-effector of a CDPR on the volume and stability of the CSS are analyzed. The analysis results can serve as guidelines for determining the CSS in practical applications. The correctness and efficacy of the proposed method are verified through the experimental and theoretical analyses. The results show that the proposed method is computationally efficient and can obtain the CSS of CDPRs within a given accuracy range.

INDEX TERMS Cable-driven parallel robots, constant stiffness space, redundant systems, stiffness.

I. INTRODUCTION

Cable-driven parallel robots (CDPRs) are used in many industrial robotics applications, and their configurations are typically similar to those of parallel manipulators. The end-effectors of these robots are driven by cables instead of rigid links [1]. The cables are almost massless and are not hampered by motion limitations of rigid rotating joints. This decreases the motion inertia of CDPRs and enables end-effectors to reach high motion accelerations in a large workspace. CDPRs have been extensively researched and are highly preferred in academic and industrial fields because of their excellent movement performance, high load capacity, and large workspace [2]–[8]. Therefore, CDPRs have attracted increasing interest for numerous applications such as material handling [9], [10] and rehabilitation [11]–[15]. However, CDPRs have certain drawbacks. As driving cables can pull but not push, redundant actuation is required to completely restrain robots, i.e., at least $m = n + 1$ cables are required to completely control a CDPR with n degrees of freedom (i.e., n-DOF CDPR). It should be noted that if gravity plays the role of an additional virtual cable, n-DOF CDPRs can be completely controlled by n cables [16]. Among the various types of CDPRs, redundantly actuated CDPRs have more actuators than the DOFs of end-effectors, with the degree of redundancy (DOR) given by $r = m - n$, where m and n are the numbers of cables and DOFs, respectively [8].

Owing to the redundant actuators, there may be numerous cable tension groups that meet the driving condition for end-effectors at a specific position. The tension of the driving cables of CDPRs strongly affects the stiffness of

The associate editor coordinating the review of this manuscript and approving it for publication was Yongping Pan.

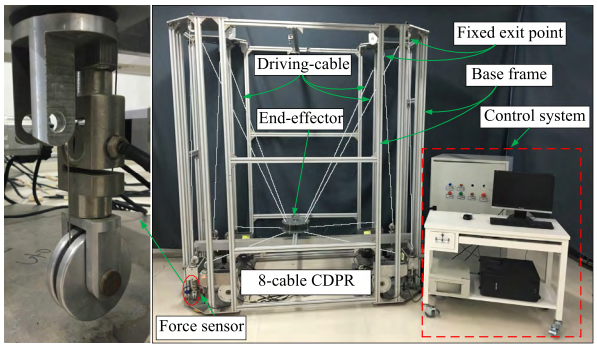

FIGURE 1. TCPR-8 CDPR prototype.

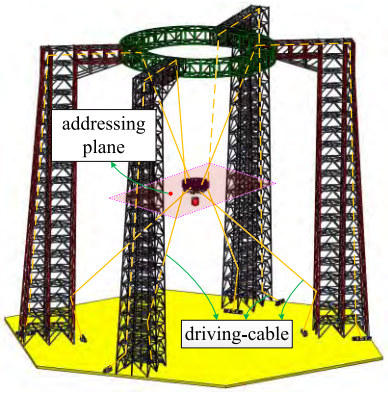

FIGURE 2. Ground simulation spacecraft Mars landing addressing experiments.

robots. This provides a condition for controlling the system stiffness of CDPRs by controlling the tension of the driving cables. Redundant actuators can improve the working space, stiffness, load capacity, etc., of CDPRs; however, they increase the number of actuators. In addition, they make the determination of the tension of driving cables more difficult (the calculation complexity increases with the DOR), and make CDPRs more complex and expensive because the cables and environment are prone to collision or interference. Considering the advantages, cost, and complexity of redundant actuation, n-DOF CDPRs are generally driven by $n + 2$ cables [17]–[20]. This study investigates the characteristics of the constant stiffness space (CSS) of redundantly actuated CDPRs with the aim of meeting the requirement for the constant stiffness plane of CDPRs in ground simulation spacecraft landing addressing experiments. Experiments were conducted on a 2-DOR, 8-cable CDPR prototype, namely, the Tsinghua cable parallel robot (TCPR-8; refer to Fig. 1). TCPR-8 is used as the a priori device for ground simulation spacecraft Mars landing addressing experiments.

The stiffness problem is an important issue that must be solved to improve the performance of robots. It is closely related to the dynamic characteristics and positioning accuracy of robots. Consequently, numerous theoretical and practical studies have been conducted in this area. In [21], the method of kinematic constraints was used to improve the system stiffness of redundant CDPRs, and the proposed approaches were experimentally tested on an actual warehousing robot. In [22], the static stiffness of the flexible-cable-driven parallel mechanism was analyzed, and two examples of static stiffness estimation were given for redundantly restrained positioning mechanism and incompletely restrained positioning mechanism (the cable-driven cabin suspension of the 500-m aperture spherical telescope), and a comparison between the analytical and simulation results proved the validity of the calculation model. According to [8], the system stiffness of redundant CDPRs could be effectively controlled by cable tension based on the cable tension feasible region (CTFR). The proposed methods were verified via theoretical analyses and experimental tests on an actual TCPR-8 robot for a simulated satellite launch. Reference [23] introduced the concept of a wrench-closure workspace (WCW) by studying planar CDPRs with different configurations, and presented the calculation method for the WCW. The method provided a useful guide to study the WCW of 6-DOF parallel cable-driven mechanisms. Reference [24] presented a hybrid analytical–numerical method to calculate the WCW by combining the high accuracy of an analytical approach and the algorithmic versatility of a numerical approach. In [25], a general approach was proposed to calculate the force-closure workspace and the method was verified through simulation. Most of the above studies attempted to enhance or control the system stiffness of CDPRs at a specific position or study the workspace of robots from the perspective of wrench/force closure.

To the best of the authors' knowledge, the workspace of robots has not been investigated from the perspective of constant stiffness until now. A spacecraft must move in a plane when addressing a suitable landing site on the surface of Mars. This plane must have a certain height with respect to the surface of Mars, and the stiffness in the plane is constant. To ensure safety, ground simulation landing experiments must be conducted before a spacecraft is launched. Ground simulation spacecraft Mars landing addressing experiments must simulate the state of the spacecraft landing on Mars as realistically as possible to ensure their validity. Therefore, as shown in Fig. 2, a spacecraft requires CDPRs with constant stiffness in the addressing plane during the experiments. This work is dedicated to solving the problem that a spacecraft must maintain constant stiffness when moving in the addressing plane. In addition, the experimental analysis is conducted using an a priori device to reduce experimental cost (see Fig. 1). The stiffness of parallel manipulators is related to their configurations, and the working space is relatively small. Thus, the requirements of ground simulation spacecraft landing addressing experiments cannot be met for a large constant-stiffness working plane. Nevertheless, the system stiffness of CDPRs can be controlled via the tension of the driving cables, and the working space is relatively large. Therefore, to meet the abovementioned requirements, it is particularly important to study the CSS of robots for continued developments in the aerospace industry.

The characteristics of 2-DOR CDPRs and the stiffness model and CTFR previously studied by the authors are reviewed. On this basis, the CSS of the redundant CDPRs is defined in this paper, and its calculation method is introduced. Then, a new index is introduced to evaluate and analyze the local and global stability of the CSS of CDPRs. The influences of the load and posture of the end-effector of CDPRs on the volume and stability of the CSS are analyzed. Finally, the correctness and validity of the proposed method are verified through theoretical analysis and two sets of experiments. Accordingly, the major contributions of this study are as follows.

(1) Based on the review of the authors' previous work on the stiffness model, the concept of the stiffness relative contribution coefficient (SRCC) is proposed, which establishes the exact relationship between controllable stiffness and its contributions to system stiffness. In addition, it can directly reflect the influence of controllable stiffness on system stiffness and guide the selection of driving cables and the setting of cable tension limiting values.

(2) According to the requirements of the ground simulation spacecraft Mars landing addressing experiments, the concept of the CSS is proposed and its detailed definition and calculation method are introduced. Additionally, two evaluation indexes, that is, the local stability factor and global stability coefficient, are proposed to evaluate and analyze the quality of the CSS.

(3) The influences of the end-effector's load and posture on the volume and stability of the CSS of CDPRs are compared and analyzed, and the correctness and efficacy of the proposed method are verified through experiments.

In addition, our findings can not only be used in the ground simulation spacecraft Mars landing addressing experiments, but also serve as a reference for researching other ground simulation spacecraft landing addressing experiments, for example, lunar or other planetary explorations.

The remainder of this paper is organized as follows. Section II reviews the stiffness model [8], [26] and CTFR previously studied by the authors [8], and introduces the concept of the SRCC. Section III defines the CSS and proposes its calculation method and evaluation index. Additionally, the effects of the load and posture of the end-effector of CDPRs on the volume and stability of the CSS are analyzed. Section IV presents the experimental verification performed using two constant stiffness planes (a rectangle and an ellipse). Finally, Section V concludes.

II. STIFFNESS MODEL

The schematic of a general CDPR model is depicted in Fig. 3. The base and moving coordinate systems O and $O^{'}$ of a CDPR are assigned, respectively. Here, A_i and B_i denote the fixed exit point of a cable and the connection point between the cable and the end-effector, respectively. By utilizing the two abovementioned coordinate systems, the position of the end-effector can be described via the position vector, $\boldsymbol{p} = [x_{O'}, y_{O'}, z_{O'}]^T$ (in meters), of the origin of $O^{'}$ in O, and

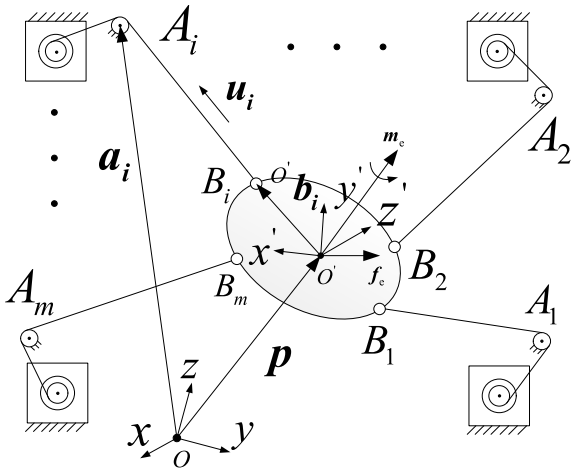

FIGURE 3. General model of CDPRs.

the posture can be described via the angular displacement, $\boldsymbol{\Theta} = [\alpha, \beta, \gamma]^T$ (in degrees), of $O^{'}$ relative to O. Thus, $\boldsymbol{x} = [\boldsymbol{p}; \boldsymbol{\Theta}]$ denotes the pose of the end-effector in O. According to the vector loop equation, the relationship between the end-effector's pose and the cable length is as follows:

$$\boldsymbol{l}_i = \boldsymbol{a}_i - \boldsymbol{p} - \boldsymbol{R} \cdot {}^{O'}\boldsymbol{b}_i \tag{1}$$

where $\boldsymbol{l}_i$ denotes the cable vector from B_i to A_i, $\boldsymbol{a}_i$ is the position vector of A_i in O, ${}^{O'}\boldsymbol{b}_i$ is the position vector of B_i in $O^{'}$, $\boldsymbol{R}$ represents the rotation matrix of $O^{'}$ relative to O, and $i = 1, 2, \cdots, m$.

When target pose $\boldsymbol{x}$ is determined, the cable length, $\|\boldsymbol{l}_i\|$ and the cable unit vector, $\boldsymbol{u}_i = \boldsymbol{l}_i / \|\boldsymbol{l}_i\|$ can be calculated using (1). The relationship between the end-effector's pose and the cable length is also determined.

The relationship between the velocity vectors of the cables and end-effector via the differentiation of (1) with respect to time can be obtained as follows:

$$\dot{\boldsymbol{l}} = -\boldsymbol{S}^T \cdot \dot{\boldsymbol{x}} \tag{2}$$

where $\dot{\boldsymbol{l}} = [\dot{\boldsymbol{l}}_1, \dot{\boldsymbol{l}}_2, \cdots, \dot{\boldsymbol{l}}_m]^T$ is the velocity vector of the cables, $\boldsymbol{S} \in R^{n \times m}$ is the structure matrix of CDPRs at a pose, and $\dot{\boldsymbol{x}} = \left[\dot{\boldsymbol{P}}, \dot{\boldsymbol{\Theta}}\right]^T$ denotes the velocity vector of the end-effector, where

$$\boldsymbol{S}(\boldsymbol{x}) = \begin{bmatrix} \boldsymbol{u}_1 & \cdots & \boldsymbol{u}_m \\ (\boldsymbol{R} \cdot {}^{O'}\boldsymbol{b}_1) \times \boldsymbol{u}_1 & \cdots & (\boldsymbol{R} \cdot {}^{O'}\boldsymbol{b}_m) \times \boldsymbol{u}_m \end{bmatrix}.$$

According to the principle of virtual work, the static equilibrium equation of CDPRs can be written as follows:

$$\boldsymbol{S}\boldsymbol{T} + \boldsymbol{W} = 0 \tag{3}$$

where $\boldsymbol{T} = [t_1, t_2, \cdots, t_m]^T$, t_i is the value of the i^{th} cable tension, $\boldsymbol{W} = \left[\boldsymbol{f}_e, \boldsymbol{m}_e\right]^T$, and $\boldsymbol{f}_e$ and $\boldsymbol{m}_e$ represent the resultant force (N) and torque ($N \cdot m$) (including the end-effector's weight) of the external environment acting on the end-effector, respectively.

Studying the stiffness of redundant CDPRs is the basis for investigating the CSS of robots. The anti-deformation ability of the end-effector under the action of external force is one of the criteria to measure system stiffness. Therefore, the relationship between the small external force, $\delta \boldsymbol{W}$, acting on the end-effector, and the small variation, $\delta \boldsymbol{x}$, in the end-effector's pose can be obtained as follows:

$$\delta \boldsymbol{W} = \boldsymbol{K} \cdot \delta \boldsymbol{x} \tag{4}$$

where $\boldsymbol{K}$ denotes the system stiffness matrix.

Using (3) and (4), the expression of the stiffness matrix is given by

$$\boldsymbol{K} = \frac{\partial \boldsymbol{W}}{\partial \boldsymbol{x}} = -(\frac{\partial \boldsymbol{S}}{\partial \boldsymbol{x}}\boldsymbol{T} + \boldsymbol{S}\frac{\partial \boldsymbol{T}}{\partial \boldsymbol{x}}) = \boldsymbol{K}_1 + \boldsymbol{K}_2 \tag{5}$$

As seen from (5), the system stiffness matrix consists of two parts. $\boldsymbol{K}_1$ is related to the structure matrix transformation and cable tension. It can be controlled by altering the cable tension at a certain pose, and it is referred to as **controllable stiffness**. $\boldsymbol{K}_2$ is related to the system structure and the end-effector's pose. It is referred to as **inherent stiffness**.

A. CONTROLLABLE STIFFNESS

Controllable stiffness is the key to controlling system stiffness and obtaining the CSS of CDPRs. This section deduces the matrix of controllable stiffness by introducing a line vector and differential transformation. From (5), $\boldsymbol{K}_1$ is written as follows:

$$\boldsymbol{K}_1 = -\boldsymbol{H}\boldsymbol{T} \tag{6}$$

where $\boldsymbol{H} = \left[\boldsymbol{H}^1, \boldsymbol{H}^2, \cdots, \boldsymbol{H}^n\right] \in R^{n\times n\times m}$ represents the three-dimensional Hessian matrix, $\boldsymbol{H}^j \in R^{n\times m}$ is the j^{th} subarray of $\boldsymbol{H}$, and

$$\boldsymbol{H}^j = \frac{\partial \boldsymbol{S}}{\partial \boldsymbol{x}_j} = \begin{bmatrix} \frac{\partial \boldsymbol{u}_1}{\partial \boldsymbol{x}_j} & \cdots & \frac{\partial \boldsymbol{u}_m}{\partial \boldsymbol{x}_j} \\ \frac{\partial\left[(\boldsymbol{R}\cdot {}^{O'}\boldsymbol{b}_1)\times \boldsymbol{u}_1\right]}{\partial \boldsymbol{x}_j} & \cdots & \frac{\partial\left[(\boldsymbol{R}\cdot {}^{O'}\boldsymbol{b}_m)\times \boldsymbol{u}_m\right]}{\partial \boldsymbol{x}_j} \end{bmatrix} \tag{7}$$

To simplify the derivation process of $\boldsymbol{H}$, the cable unit vector, $\boldsymbol{u}_i$, is written with the direction cosine as follows:

$$\boldsymbol{u}_i = [c\alpha_i, c\beta_i, c\gamma_i]^T \tag{8}$$

where α_i, β_i, and γ_i denote the angle of $\boldsymbol{u}_i$ about the Cartesian axis x, y, and z, respectively.

(Note: To simplify the expression, we use $c\theta$ and $s\theta$ instead of $cos\theta$ and $sin\theta$, respectively, in this paper.)

From (7) and (8), the partial derivatives of $\boldsymbol{u}_i$ and $(\boldsymbol{R}\cdot {}^{O'}\boldsymbol{b}_i)\times \boldsymbol{u}_i$ with respect to $\boldsymbol{x}_j$ can be obtained as follows:

$$\frac{\partial \boldsymbol{u}_i}{\partial \boldsymbol{x}_j} = \frac{\partial \boldsymbol{u}_i}{\partial \boldsymbol{\alpha}_i}\frac{\partial \boldsymbol{\alpha}_i}{\partial \boldsymbol{x}_j} + \frac{\partial \boldsymbol{u}_i}{\partial \boldsymbol{\beta}_i}\frac{\partial \boldsymbol{\beta}_i}{\partial \boldsymbol{x}_j} + \frac{\partial \boldsymbol{u}_i}{\partial \boldsymbol{\gamma}_i}\frac{\partial \boldsymbol{\gamma}_i}{\partial \boldsymbol{x}_j} \tag{9}$$

$$\frac{\partial\left[(\boldsymbol{R}\cdot {}^{O'}\boldsymbol{b}_i)\times \boldsymbol{u}_i\right]}{\partial \boldsymbol{x}_j} = \frac{\partial(\boldsymbol{R}\cdot {}^{O'}\boldsymbol{b}_i)}{\partial \boldsymbol{x}_j}\times \boldsymbol{u}_i + (\boldsymbol{R}\cdot {}^{O'}\boldsymbol{b}_i)\times \frac{\partial \boldsymbol{u}_i}{\partial \boldsymbol{x}_j} \tag{10}$$

As $\boldsymbol{R}' = \boldsymbol{\omega}\times \boldsymbol{R}$, using (1), the following expression can be obtained:

$$\begin{aligned} \dot{\boldsymbol{l}}_i\cdot \boldsymbol{u}_i + \boldsymbol{l}_i\cdot \dot{\boldsymbol{u}}_i &= -\dot{\boldsymbol{p}} - \boldsymbol{\omega}\times(\boldsymbol{R}\cdot {}^{O'}\boldsymbol{b}_i) \\ &= \left[-\boldsymbol{I}\left(\boldsymbol{R}\cdot {}^{O'}\boldsymbol{b}_i\right)^{\times}\right]\dot{\boldsymbol{x}} = \boldsymbol{G}_i\dot{\boldsymbol{x}} \end{aligned} \tag{11}$$

where $\boldsymbol{G}_i \in R^{3\times 6}$ denotes the algebraic matrix.

From (2), we obtain the following:

$$\dot{\boldsymbol{l}}_i = -\boldsymbol{S}_i^T\dot{\boldsymbol{x}} \tag{12}$$

where $\boldsymbol{S}_i^T$ is the i^{th} row vector of $\boldsymbol{S}^T$.

Using (12), we obtain the following:

$$\dot{l}_i\boldsymbol{u}_i = -\begin{bmatrix} c\alpha_i\cdot \boldsymbol{S}_i^T \\ c\beta_i\cdot \boldsymbol{S}_i^T \\ c\gamma_i\cdot \boldsymbol{S}_i^T \end{bmatrix}\dot{\boldsymbol{x}} = \boldsymbol{Q}_i\dot{\boldsymbol{x}} \tag{13}$$

where $\boldsymbol{Q}_i \in R^{3\times 6}$ represents the algebraic matrix.

Substituting (13) into (11), we obtain the following:

$$\begin{cases} \frac{\partial \alpha_i}{\partial x_j} = -\frac{1}{l_i\cdot s\alpha_i}\left[\boldsymbol{G}_i - \boldsymbol{Q}_i\right]_{1,j} \\ \frac{\partial \beta_i}{\partial x_j} = -\frac{1}{l_i\cdot s\beta_i}\left[\boldsymbol{G}_i - \boldsymbol{Q}_i\right]_{2,j} \end{cases} \tag{14}$$

where $\left[\boldsymbol{G}_i - \boldsymbol{Q}_i\right]_{1,j}$ and $\left[\boldsymbol{G}_i - \boldsymbol{Q}_i\right]_{2,j}$ are the elements of the first row and j^{th} column and the second row and j^{th} column of matrix $\left[\boldsymbol{G}_i - \boldsymbol{Q}_i\right]$, respectively.

Through the derivatives of $\boldsymbol{R}\cdot {}^{O'}\boldsymbol{b}_i$ with respect to time, we obtain the following:

$$\frac{\partial\left(\boldsymbol{R}\cdot {}^{O'}\boldsymbol{b}_i\right)}{\partial \boldsymbol{x}_j} = \boldsymbol{M}_{i,j} \tag{15}$$

where $\boldsymbol{M}_i \in R^{3\times 6}$ is the algebraic matrix and $\boldsymbol{M}_{i,j}$ denotes the j^{th} column vector of $\boldsymbol{M}_i$.

$\boldsymbol{H}$ can be obtained by substituting (14) and (15) into (9), (10), and (7). The stiffness matrix $\boldsymbol{K}_1$ can be calculated using (6) and the cable tension vector $\boldsymbol{T}$.

B. INHERENT STIFFNESS

Even though inherent stiffness is not controlled by cable tension, it has a significant impact on system stiffness. Therefore, this section presents the process of deducing the matrix of inherent stiffness. Using (5), we obtain the following:

$$\boldsymbol{K}_2 = -\boldsymbol{S}\frac{\partial \boldsymbol{T}}{\partial \boldsymbol{l}}\frac{\partial \boldsymbol{l}}{\partial \boldsymbol{x}} \tag{16}$$

The relationship between the deformation and tension of the cables is expressed as follows:

$$\frac{\partial \boldsymbol{T}}{\partial \boldsymbol{l}} = diag(\frac{\mathrm{E}_1\cdot \mathrm{A}_1}{l_{\mathrm{o}1}}, \cdots, \frac{\mathrm{E}_m\cdot \mathrm{A}_m}{l_{\mathrm{o}m}}) \tag{17}$$

where E_i, A_i, and l_{oi} are the elastic modulus, cross-sectional area, and static length of a cable, respectively.

Using (2), we obtain the following:

$$\frac{\partial \boldsymbol{l}}{\partial \boldsymbol{x}} = -\boldsymbol{S}^T \tag{18}$$

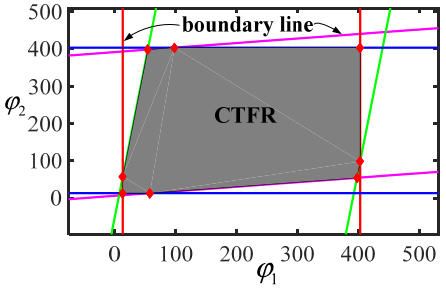

FIGURE 4. CTFR of TCPR-8 at pose $x = [0, 0, 0.83, 0, 0, 0]^T$, and the load of its end-effector is zero. $t_{min} = 10\ N$ and $t_{max} = 400\ N$.

Substituting (17) and (18) into (16), we obtain

$$\boldsymbol{K}_2 = \boldsymbol{S} \cdot diag(\frac{\mathrm{E}_1 \cdot \mathrm{A}_1}{l_{o1}}, \cdots, \frac{\mathrm{E}_m \cdot \mathrm{A}_m}{l_{om}}) \cdot \boldsymbol{S}^T \tag{19}$$

The stiffness matrix of controllable stiffness $\boldsymbol{K}_1$ and inherent stiffness $\boldsymbol{K}_2$ can be calculated using the above equations, and system stiffness $\boldsymbol{K}$ can be obtained.

C. CABLE TENSION FEASIBLE REGION

From Section II.A, it is clear that the controllable stiffness of CDPRs can be adjusted by altering the cable tension. Therefore, the CSS of CDPRs is studied based on the CTFR. Taking 2-DOR CDPRs as an example, when the external load of the end-effector is constant, the CTFR is obtained while satisfying system balance and preventing cable slack or overload.

As this work focuses on the problem of the CSS for 2-DOR CDPRs ($r = m - n = 2$), $\boldsymbol{S}$ is a nonsquare matrix. When $\boldsymbol{S}$ is a full-rank matrix, (3) is equivalent to the following well-known equation:

$$\boldsymbol{T} = \boldsymbol{S}^{+}(-\boldsymbol{W}) + \boldsymbol{N}\boldsymbol{\varphi} = \boldsymbol{t}_p + \boldsymbol{t}_n \tag{20}$$

where $\boldsymbol{S}^{+} = \boldsymbol{S}^T(\boldsymbol{S}\boldsymbol{S}^T)^{-1}$ is the pseudo-inverse of matrix $\boldsymbol{S}$, $\boldsymbol{N} = \mathrm{null}(\boldsymbol{S})$ denotes a full-rank $m \times r$ matrix, the two columns of $\boldsymbol{N}$ form an orthonormal basis of the null-space of $\boldsymbol{S}$, $\boldsymbol{\varphi} = [\varphi_1\ \varphi_2]^T$ is an arbitrary 2D vector representing one point, $\varphi_1 \in R$, $\varphi_2 \in R$, $\boldsymbol{S}^{+}(-\boldsymbol{W})$ represents the minimum-norm solution of (3), $\boldsymbol{N}\boldsymbol{\varphi}$ is the homogeneous general solution of (3), $\boldsymbol{t}_p = \boldsymbol{S}^{+}(-\boldsymbol{W})$, and $\boldsymbol{t}_n = \boldsymbol{N}\boldsymbol{\varphi}$.

$\boldsymbol{\phi}$ denotes the set of tension solutions, $\boldsymbol{T}$, for (3), satisfying the inequalities $t_{\min} \le t_i \le t_{\max}$, which can be defined via the following set of 2m linear inequalities:

$$t_{\min} - \boldsymbol{t}_p \le \boldsymbol{N}_{m\times 2}\boldsymbol{\varphi} \le t_{\max} - \boldsymbol{t}_p \tag{21}$$

where $t_{\min}$ and $t_{\max}$ are the minimum and maximum limiting values of cable tension, respectively. When $t_{\min}$ and $t_{\max}$ are determined, each inequality defines a half plane through a boundary line with $\boldsymbol{\varphi}$ changes. The intersection of 2m half planes given by (21) forms a closed region, which is the CTFR. An example of the CTFR is shown in Fig. 4.

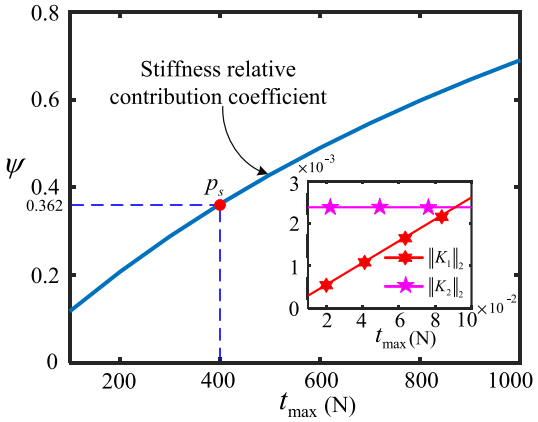

FIGURE 5. Variation curves of the stiffness relative contribution coefficient.

D. STIFFNESS RELATIONSHIP AND MEASUREMENT METHOD

The system stiffness of redundant CDPRs can be controlled by cable tension, and it is positively correlated with the same. At a specific pose, inherent stiffness and its contribution to system stiffness are constant, and controllable stiffness and its contribution to system stiffness change with cable tension. The SRCC, ψ, used to measure the contribution of controllable stiffness to system stiffness, is expressed as follows:

$$\psi = \frac{\|K_1\|_2}{\|K\|_2} \tag{22}$$

where $\|K_1\|_2$ and $\|K\|_2$ represent the 2-norms of K_1 and K, respectively.

Considering the pose of the end-effector of TCPR-8, $\boldsymbol{x} = [0, 0, 0.83, 0, 0, 0]^T$ as an example, the robot is controlled by the cable tension at the centroid of the CTFR. The variations in ψ, $\|K_1\|_2$, and $\|K_2\|_2$ with $t_{\max}$ are illustrated in Fig. 5. The figure indicates that ψ is a monotonically increasing function greater than 0, because inherent stiffness is constant and controllable stiffness increases with cable tension. ψ tends to 0 when $t_{\max}$ is relatively small. At this time, controllable stiffness contributes negligibly to system stiffness, and system stiffness is approximately equal to inherent stiffness. The figure also shows that (22) establishes the exact relationship between controllable stiffness and its contributions to system stiffness. In practical applications, (22) can be used to select the corresponding $t_{\max}$ according to the requirement for the stiffness adjustment range, and then, the appropriate driving cable can be selected according to $t_{\max}$.

Therefore, to improve the influence of controllable stiffness on system stiffness and increase the control range of cable tension to controllable stiffness, this study selects $\psi = 0.362$ based on the load conditions of the cables and drivers and the corresponding cable tension limiting value is $t_{\max} = 400\,N$, as shown in Fig. 5.

To effectively measure the variation in system stiffness and analyze the CSS of CDPRs, this study adopts the method involving "the relationship between external force and the

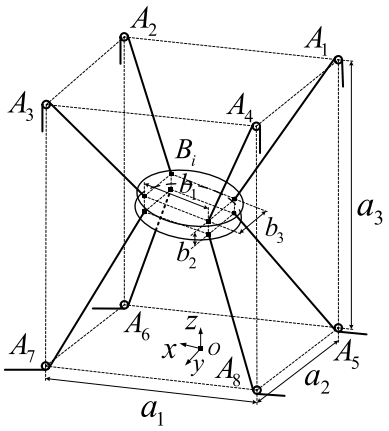

FIGURE 6. Configuration of TCPR-8.

TABLE 1. Dimensions of TCPR-8 (in meters).

Dimension	Value	Dimension	Value
a_1	1.540	b_1	$0.124\sqrt{2}$
a_2	1.032	b_2	$0.124\sqrt{2}$
a_3	1.780	b_3	0.085

change in the pose of the end-effector'' proposed by the authors in [8]. Under the same external force, the larger the changes in the pose of the end-effector, the smaller the system stiffness at a certain pose, and vice versa.

From (4), we obtain the following:

$$\Delta \boldsymbol{x} = \boldsymbol{K}^{-} \cdot \boldsymbol{W} \tag{23}$$

where $\Delta \boldsymbol{x} = \left[\Delta x_{O'}, \Delta y_{O'}, \Delta z_{O'}, \Delta\alpha, \Delta\beta, \Delta\gamma\right]^T$ denotes the value of the change in pose, and $\boldsymbol{K}^{-} = \left(\boldsymbol{K}^T\boldsymbol{K}\right)^{-1} \cdot \boldsymbol{K}^T$ is the generalized inverse matrix of $\boldsymbol{K}$.

According to the external load of the end-effector, the change in the pose of the end-effector at a certain pose can be calculated using (23), following which the CSS of CDPRs can be examined.

III. CALCULATION AND ANALYSIS OF CONSTANT STIFFNESS SPACE

A prototype of TCPR-8 is utilized in this study to verify the correctness and validity of the proposed concepts and methods. Fig. 1 illustrates the prototype of the studied 6-DOF CDPR designed for a simulated satellite launch. The cable layout and dimensions of the fixed and end-effector of the CDPR are shown in Fig. 6 and Table 1, respectively. Table 2 summarizes the mechanical properties of the robot.

A. DEFINITION AND CALCULATION OF CONSTANT STIFFNESS SPACE

When designing a CDPR system, the corresponding requirements for vibration and stability during the movement of the end-effector are typically proposed. One such requirement is that robots must have constant stiffness, particularly in the

TABLE 2. Mechanical properties and Rope Cross-section Diameter of TCPR-8.

Parameter	Description	Value
D	Cross-section diameter of cables	0.472 mm
E_s	Young modulus of elasticity of cables	12.4 Gpa
$t_{\max}$	Maximum cable tension	400 N
$t_{\min}$	Minimum cable tension	10 N
m	end-effector mass	2 kg

context of the ground simulation spacecraft landing addressing experimental platform system. As the cable tension and poses of redundant CDPRs are coupled to each other, and redundant CDPRs have an infinite number of feasible cable tensions at a specific position, the system stiffness of robots can be maintained as constant by controlling the cable tension based on the CTFR, which is the main focus of this work. The closed area with constant stiffness formed by the set of poses with cable tension belonging to the CTFR is referred to as the **constant stiffness space** (CSS), and it is expressed as follows:

$$\begin{aligned} &find \;\; V(x) \\ &\text{subject to} \;\; K(\mathrm{x}_i) = k_c \qquad (24a) \\ &\qquad\qquad \boldsymbol{\varphi}_x \in CTFR(x_i) \qquad (24b) \end{aligned}$$

where $V(x)$ denotes the CSS, x is the set of poses of the CDPRs, $K(\mathrm{x}_i)$ is the system stiffness of CDPRs at pose x_i, x_i is any pose in set x, k_c represents a constant matrix, $CTFR(x_i)$ denotes the CTFR of CDPRs at pose x_i, and $\boldsymbol{\varphi}_x$ is an arbitrary point in the plane of $CTFR(x_i)$.

The calculation method for the CSS of the CDPRs is introduced based on the CTFR to quickly and effectively determine the CSS. The calculation process is shown in Fig. 7. The steps are as follows:

Step 1: Input the mechanism design parameters and required accuracy ε.

Step 2: The envelope space, S_o, formed by the fixed exit point of the cable is meshed with a reasonable step size, s_l, in the x, y, and z directions. n grid points are obtained, and the pose, x_i, of the end-effector at any grid point can be determined according to the angular displacement of the end-effector.

Step 3: The stiffness matrix, k_c, of the CSS is calculated according to the requirements.

Step 4: Let $i = 1$.

Step 5: Search for point $\boldsymbol{\varphi}_x$ in the plane where the $CTFR(x_i)$ is located such that $\left|k\left(T(\boldsymbol{\varphi}_x)\right) - k_c\right| / k_c \leq \varepsilon$, where $k\left(T(\boldsymbol{\varphi}_x)\right)$ is the system stiffness matrix of the robots controlled by cable tension $T(\boldsymbol{\varphi}_x)$.

Step 6: If $\boldsymbol{\varphi}_x \in CTFR(x_i)$, x_i is added to set $V(x)$; otherwise, the next step is executed.

Step 7: If $i < n$, then $i = i + 1$ and Step 5 is executed; otherwise, $V(x)$ is output.

Step 8: End.

In this work, accuracy $\varepsilon = 5\%$ and step size $s_l = 1$ mm.

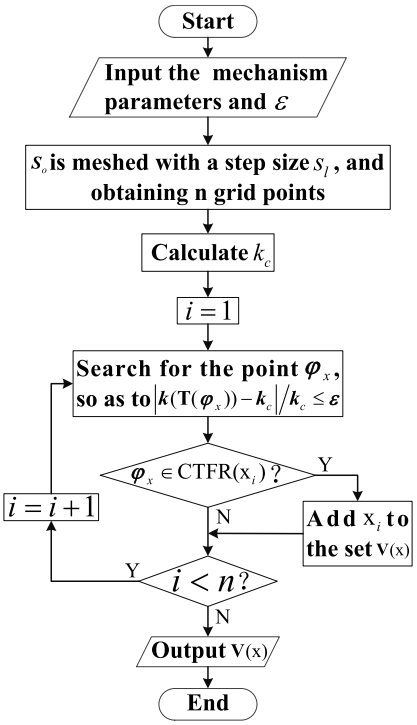

FIGURE 7. Flowchart of the CSS algorithm.

After obtaining the CSS of the CDPRs using the above-mentioned method, any pose in the CSS corresponds to a set of driving cable tensions. The CDPRs can maintain constant stiffness when controlled by the driving cable tension. Therefore, CDPRs can maintain constant stiffness when working in the CSS by controlling the cable tension of the driving cables.

B. QUALITY EVALUATION INDEX FOR CONSTANT STIFFNESS SPACE

The volume and stability of the CSS of the CDPRs are important indexes for measuring its quality. Undesirable motion characteristics, such as vibration, may occur during the movement of robots in a large CSS. Therefore, studying the stability distribution of the CSS plays an important role in investigating the trajectory planning of robots. The stability of cable tension directly affects the stability of the CDPRs. If the tension of the driving cables is less than the minimum limiting value, then the driving cables are prone to pseudo-drag or vibration. If the tension of the driving cables is more than the maximum limiting value, then the motors or driving cables are prone to overload. Therefore, the cable tensions that are far from the limiting values are considered to be stable and safe. Thus, the local stability factor, μ_i, and the global stability coefficient, U, are used as the evaluation indexes for the stability and safety of the CSS of CDPRs, and they are expressed as follows:

$$\mu_i = \frac{1}{m}\sum_{k=1}^{m}\frac{|t_{ik}-\bar{t}|}{\bar{t}} \tag{25a}$$

TABLE 3. Cable tension at the centroid of the CTFR (in newton).

Driving cables	Cable tension	Driving cables	Cable tension
Cable1	193.7	Cable5	210.3
Cable2	193.7	Cable6	210.3
Cable3	193.7	Cable7	210.3
Cable4	193.7	Cable8	210.3

$$\mathrm{U} = \frac{\int_v \mu_i dv}{\int_v dv} \tag{25b}$$

where $\boldsymbol{T}_i = [t_{i1}, \cdots, t_{ik}, \cdots, t_{im}]^T$, t_{ik} represents the value of the k^{th} cable tension at pose x_i, $\bar{t} = (t_{\max} - t_{\min})/2$ is the median of the cable tension limiting values, and v denotes the volume of the CSS. μ_i is the stability evaluation index of robots at pose x_i, which reflects the local stability of a pose within the CSS, and U reflects the global stability of the CSS. From (25a), we can conclude that μ_i is a nonnegative real number not greater than 1. At pose x_i, the smaller the value of μ_i, the farther the cable tension of CDPRs from the limiting values of cable tension and the higher the stability of the CDPRs. The larger the value of μ_i, the closer the cable tension of the CDPRs from the limiting values of cable tension, and the lower the stability of the CDPRs. Moreover, the driving cable is more prone to pseudo-drag or overload. $0 \le \mu_i \le 1 \Rightarrow 0 \le \int_v \mu_i dv \le \int_v dv \Rightarrow 0 \le U \le 1$. Therefore, the smaller the value of U, the better the global stability of the CSS, and vice versa.

C. INFLUENCE OF LOAD ON CONSTANT STIFFNESS SPACE

Robots are used in different work situations, and end-effectors must bear different loads. A robot's load is closely related to its CSS. Therefore, to meet the requirement for the CSS when robots experience different external loads, this study investigates the influence of the load of a CDPR (considering TCPR-8 as an example) on its CSS. To analyze the CSS of the CDPR under different loads, the system stiffness matrix of TCPR-8, which is controlled by the cable tension (the tension of each driving cable is shown in Table 3) at the centroid of the CTFR, is considered as the stiffness matrix of the CSS when the end-effector of TCPR-8 is at pose $x = [0, 0, 0.83, 0, 0, 0]^T$ and its external load is zero. Using (5), etc., the system stiffness matrix of TCPR-8 can be obtained as follows:

$$k = \begin{Bmatrix} 6055.06 & 0.0 & 0.0 & 0.0 & -267.81 & 0.0 \\ 0.0 & 3226.71 & 0.0 & 137.46 & 0.0 & 0.0 \\ 0.0 & 0.0 & 8379.21 & 0.0 & 0.0 & 0.0 \\ 0.0 & 137.46 & 0.0 & 150.83 & 0.0 & 0.0 \\ -267.81 & 0.0 & 0.0 & 0.0 & 177.17 & 0.0 \\ 0.0 & 0.0 & 0.0 & 0.0 & 0.0 & 162.21 \end{Bmatrix} \tag{26}$$

To study the influence of the end-effector with different loads on the volume and stability of the CSS of the CDPR, the system stiffness of the CSS is considered as k.

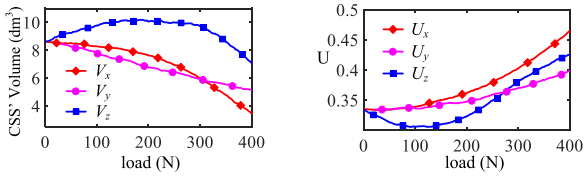

FIGURE 8. Change in volume and stability of CSS with forces in different directions. (a) Curves of CSS volume. (b) Curves of CSS stability.

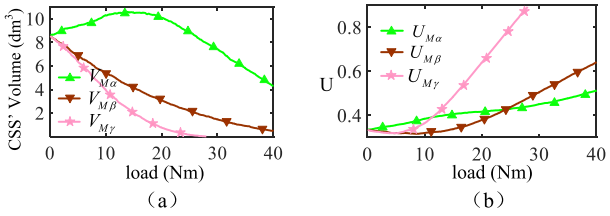

FIGURE 9. Change in volume and stability of CSS with torques in different directions. (a) Curves of CSS volume. (b) Curves of CSS stability.

TABLE 4. Four cases of different loads.

Case	Load	Case	Load
Case 1	$[5,5,5,0.5,0.5,0.5]^T$	Case 3	$[15,15,15,1.5,1.5,1.5]^T$
Case 2	$[10,10,10,1,1,1]^T$	Case 4	$[20,20,20,2,2,2]^T$

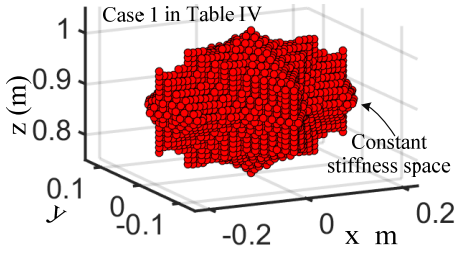

FIGURE 10. Constant stiffness space.

Then, the variation in the volume and stability of the CSS with the load force or torque in a particular direction (the load force or torque in the remaining directions are zero) are obtained using the idea of control variables. The variation curves are illustrated in Figs. 8 and 9. A section of the CSS is considered as an example to analyze the influence of the end-effector with different loads on the local stability of the CSS. Then, the stability of the CSS is compared for four different cases, as presented in Table 4. Among them, taking case 1 in Table 4 as an example, the shape of the CSS is shown in Fig. 10. The distribution of the local stability factor of the CSS on section z = 0.89 for all four cases is shown in Fig. 11. The volumes and global stability coefficients of the CSS for all four cases are provided in Table 5.

The results shown in Figs. 8 and 9 and Table 5 indicate that as the end-effector's load increases, the volume of the CSS of the CDPR decreases gradually until it becomes zero and the stability of the CSS gradually deteriorates. Therefore, the appropriate CSS can be determined according to the robots' requirements for load and stability. It is worth noting that as the load in the z and α directions increases, the volume of the CSS of the CDPR first increases and then decreases. In addition, as the load in the z direction increases, the stability of the CSS first increases and then decreases. This is mainly caused by the anisotropy of the mechanical properties of the CDPR. Therefore, within a certain range, we can utilize the characteristics of CDPRs to increase the volume and stability of the CSS by increasing the load of the robots in the z or α direction.

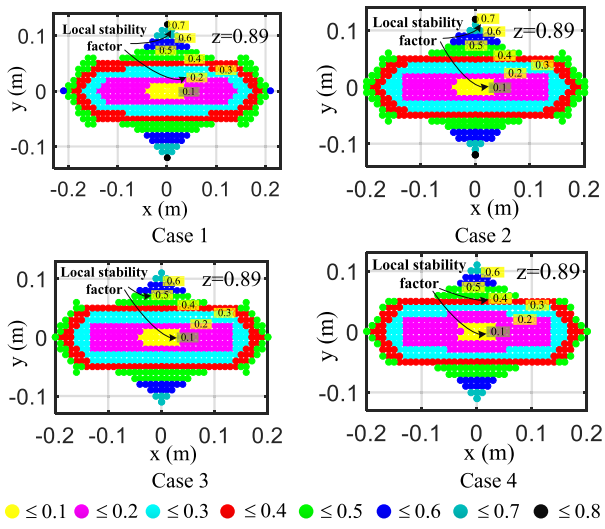

FIGURE 11. Local stability factor distribution in the CSS section for all cases in table 4.

TABLE 5. Volumes and global stability coefficients of the CSS for all cases in table IV.

Case	Volume	U
Case 1	$8.608\times10^{-3}m^3$	0.3292
Case 2	$8.408\times10^{-3}m^3$	0.3225
Case 3	$8.160\times10^{-3}m^3$	0.3160
Case 4	$8.024\times10^{-3}m^3$	0.3136

The results shown in Fig. 11 indicate that the volume of the CSS decreases with the increase in load. It can also be concluded that the local stability factor gradually increases from the center to the edge of the CSS, which indicates that the stability at the center of the CSS is better than that at the edges. To ensure the stability of robots in practical applications, the center area of the CSS located away from the boundary must be selected as a priority.

D. INFLUENCE OF POSTURE ON CONSTANT STIFFNESS SPACE

Similar to loads, different work situations require end-effectors with different postures. The postures of the end-effectors of robots are closely related to their CSS.

TABLE 6. Cable tension at the Centroid of the CTFR (in newton).

Driving cables	Cable tension	Driving cables	Cable tension
Cable1	192.4	Cable5	222.1
Cable2	189.9	Cable6	208.1
Cable3	190.8	Cable7	213.1
Cable4	182.2	Cable8	212.4

TABLE 7. Four cases of different postures.

Case	Case 1	Case 2	Case 3	Case 4
posture	$[1,1,1]^T$	$[2,2,2]^T$	$[3,3,3]^T$	$[4,4,4]^T$

Therefore, to meet the requirement for the CSS when robots have different postures, research on the influence of the posture of the end-effector of a CDPR (considering TCPR-8 as an example) on its CSS is conducted. To analyze the CSS of the CDPR under different postures, the system stiffness matrix of TCPR-8, which is controlled by the cable tension (the tension of each driving cable is shown in Table 6) at the centroid of the CTFR, is considered as the stiffness matrix of the CSS when the end-effector of TCPR-8 is at pose $x = [0, 0, 0.83, 0, 0, 0]^T$ and its external load is $W = [5, 5, 5, 0.5, 0.5, 0.5]^T$. From (5), etc., the system stiffness matrix of TCPR-8 can be obtained as follows:

$$k = \begin{Bmatrix} 6052.17 & -4.94 & -7.19 & -0.11 & -269.58 & 0.90 \\ -4.94 & 3224.07 & 0.83 & 139.10 & 0.17 & -0.71 \\ -7.19 & 0.83 & 8379.79 & -0.57 & 0.84 & -0.06 \\ -0.11 & 139.10 & -0.57 & 151.72 & -0.97 & -1.29 \\ -269.58 & 0.17 & 0.84 & -1.47 & 178.01 & 0.32 \\ 0.30 & -0.71 & -0.06 & -0.79 & -0.18 & 161.93 \end{Bmatrix} \tag{27}$$

To study the influence of the different postures of the end-effector on the volume and stability of the CSS of the CDPR, the variation in the volume and stability of the CSS with angular displacement of posture in a specific direction (the angular displacement in the remaining directions is zero) is obtained by using methods similar to those described in Section III.C. The variation curves are shown in Fig. 12. The stability of a section of the CSS is considered as an example to analyze the influence of the different postures of the end-effector on the local stability of the CSS, and four different cases are considered, as shown in Table 7. Among them, taking case 1 in Table 7 as an example, the shape of the CSS is illustrated in Fig. 14. The distribution of the local stability factor of the CSS on section $z = 0.89$ for all four cases is presented in Fig. 13. The volumes and global stability coefficients of the CSS for all four cases are provided in Table 8.

The results shown in Fig. 12 and Table 8 indicate that as the angular displacement of the end-effector's posture increases, the volume of the CSS of the CDPR decreases gradually until it becomes zero and the stability of the CSS gradually deteriorates. Therefore, to ensure the stability of

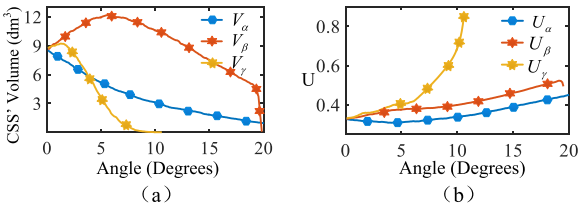

FIGURE 12. Variation in volume and stability of CSS with angular displacement in different directions. (a) Curves of CSS volume. (b) Curves of CSS stability.

TABLE 8. Volumes and global stability coefficients of the CSS for all cases in table VII.

Case	Volume	U
Case 1	$9.448\times10^{-3}\,m^3$	0.3418
Case 2	$8.120\times10^{-3}\,m^3$	0.3548
Case 3	$5.232\times10^{-3}\,m^3$	0.3614
Case 4	$2.776\times10^{-3}\,m^3$	0.3782

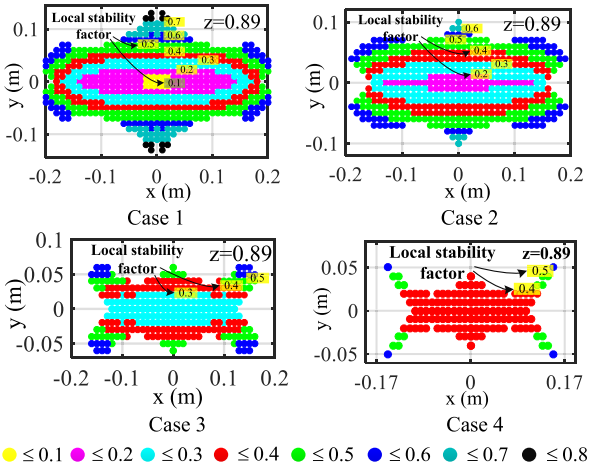

FIGURE 13. Local stability factor distribution in the CSS section for all cases in table 7.

robots within the CSS, large angular displacement of the end-effector's posture should be avoided as much as possible. Note that as the angular displacement in the β and γ directions increases, the volume of the CSS of the CDPR first increases and then decreases. This is mainly caused by the anisotropy of the mechanical properties of the CDPR. Similarly, within a certain range, we can utilize the characteristics of CDPRs to increase the volume of the CSS by increasing the angular displacement of the end-effector's posture in the β and γ directions. Similar to Section III.C, the results shown in Fig. 13 indicate that the volume of the CSS decreases with the increase in the angular displacement of the end-effector's posture. It can also be concluded that the local stability factor gradually increases from the center to the edge of the CSS, which indicates that the stability at the center of the CSS is better than that at the edges.

The results described in Sections III.C and III.D are summarized below.

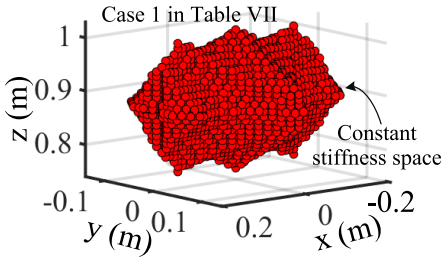

FIGURE 14. Constant stiffness space.

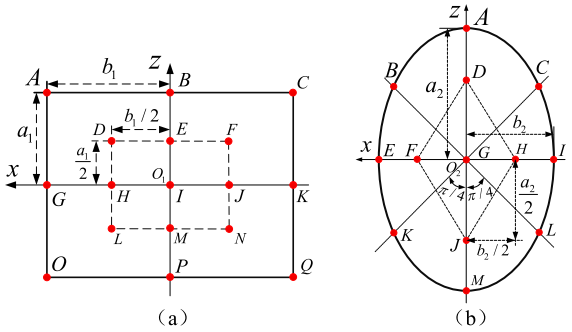

FIGURE 15. Constant stiffness planes. (a) Rectangle. (b) Ellipse.

(1) In general, as the load and angular displacement of the end-effector's posture increase, the volume of the CSS of CDPRs decreases and the stability gradually deteriorates. However, the volume of the CSS of CDPRs can be increased by increasing load or the angular displacement of the end-effector's posture within a certain range.

(2) The stability of the CSS gradually deteriorates from the center to the edge.

IV. EXPERIMENTAL VERIFICATION AND DISCUSSION

The proposed concepts and methods are verified experimentally. For this purpose, two planes are selected in the CSS of TCPR-8 when the angular displacement of the end-effector's posture is $\Theta = [0, 0, 0]^T$. The position and dimensions of the planes are shown in Fig. 15 and Table 9. In each experiment, a Leica AT901-B laser tracker measurement system, whose precision is 0.001 mm, is used to measure the change in the end-effector's pose. Heavy objects are hung on the end-effector to provide a constant external load of 10 N. The driving cable tension is recorded using a DJSX-44-100KG S-type pull pressure sensor. Figs. 16 and 1 show the details of the measurement systems and hanging objects.

In the first experiment, the end-effector is at position O_1 and its external load is 10 N in the x direction. The system stiffness matrix of TCPR-8, which is controlled by the cable tension at the centroid of the CTFR, is considered as the stiffness matrix of constant stiffness plane $S_{c1}(ACQO)$, which is a rectangle with center O_1, as illustrated in Fig. 15(a).

To make the stiffness of S_{c1} constant, TCPR-8 is controlled via suitable cable tension in the CTFR, which can be obtained by utilizing the methods described in Section III.A. As the cable tension surface information of each cable is similar, the cable tension surface of the first and eighth cables is considered as an example for illustration, as shown in Fig. 17. As illustrated in Fig. 15(a), 17 points (A, B, $\cdots$, I, $\cdots$, P, Q etc.) are selected in S_{c1} for experimental verification, and 17 sets of experimental cable tension values for controlling TCPR-8 are obtained, as shown in Fig. 17. The pose change values (Δx_A,

TABLE 9. Position and dimensions of constant stiffness planes (in meters).

Dimension	Value	Dimension	Value
a_1	0.06	a_2	0.08
b_1	0.04	b_2	0.04
O_1	(0,0,0.89)	O_2	(0,0,0.89)

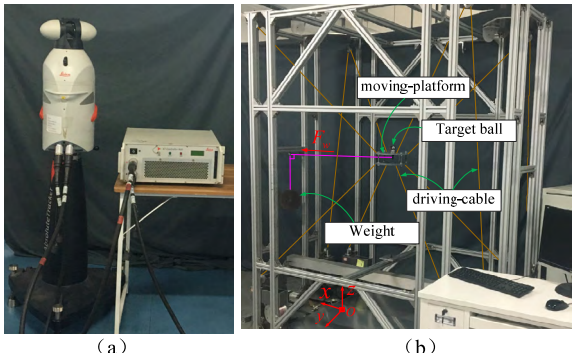

FIGURE 16. (a) Leica AT901-B laser tracker. (b) Hanging heavy objects.

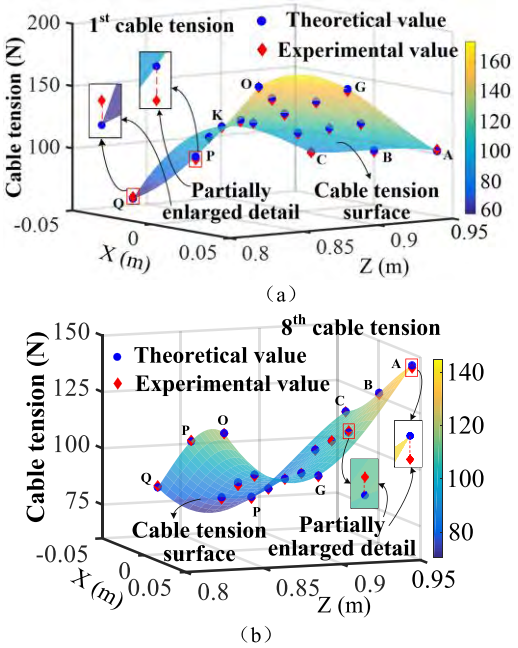

FIGURE 17. Change surface of cable tension: 1st experiment. (a) First cable. (b) Eighth cable.

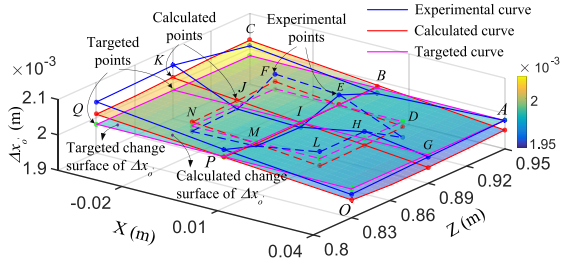

FIGURE 18. Comparison curves between calculated, experimental, and targeted $\Delta x_{O'}$.

TABLE 10. Comparison of calculated, experimental, and targeted values of pose change in x direction (in millimeters).

Position	Pose change			
	Calculated	Relative error	Experimental	Relative error
A	1.953	1.42%	1.981	0
B	1.985	0.20%	1.966	0.76%
C	2.026	2.27%	2.009	1.41%
D	1.966	0.76%	1.936	2.27%
E	1.983	0.10%	2.01	1.46%
F	2.002	1.06%	2.023	2.12%
G	1.944	1.87%	1.974	0.35%
H	1.961	1.01%	2.001	1.01%
I	1.979	0.10%	1.967	0.71%
J	1.997	0.81%	1.974	0.35%
K	2.017	1.82%	2.052	3.60%
L	1.961	1.01%	2.001	1.01%
M	1.977	0.81%	1.973	0.40%
N	1.993	0.61%	1.967	0.71%
O	1.951	1.51%	1.966	0.76%
P	1.981	0	2.001	1.01%
Q	2.011	1.51%	2.044	3.18%

$\Delta x_B, \ldots, \Delta x_I, \ldots, \Delta x_P$, and Δx_Q) in the x direction are recorded using the laser tracker under the control of the 17 sets of cable tension. The calculated, experimental, and targeted values (the targeted change value is 1.9809 in the x direction) of pose change are compared, as illustrated in Fig. 18 and Table 10.

In the second experiment, the end-effector is at position O_2 and its external load is 10 N in the y direction. The system stiffness matrix of TCPR-8, which is controlled by the cable tension at the centroid of the CTFR, is considered as the stiffness matrix of constant stiffness plane S_{k2}(AIME), which is an ellipse with center O_2, as illustrated in Fig. 15(b).

To make the stiffness of S_{k2} constant, TCPR-8 is controlled via suitable cable tension within the CTFR, which can be accomplished by employing the methods described in Section III.A. This experiment also considers the cable tension surface of the first and eighth cables as an example for illustration, as shown in Fig. 19. As illustrated in Fig. 15(b), 13 points (A, B, $\cdots$, G, $\cdots$, L, M, etc.) are selected in S_{k2} for experimental verification, and 13 sets of

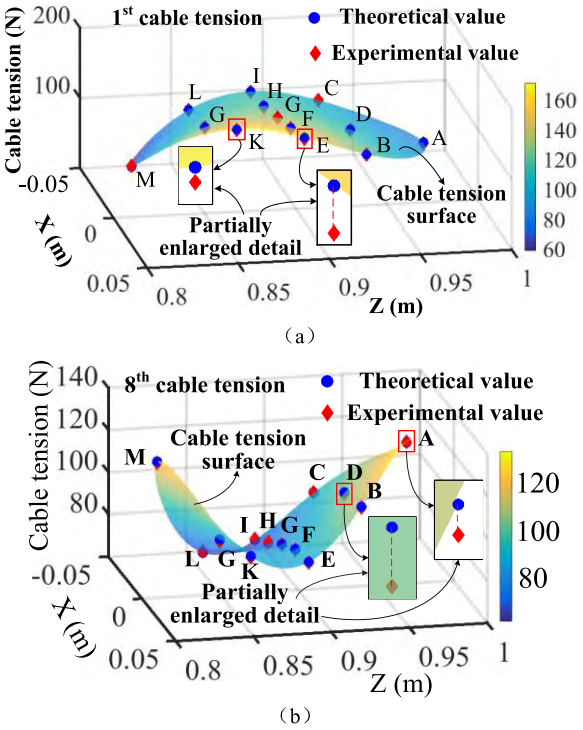

FIGURE 19. Change surface of cable tension: 2nd experiment. (a) First cable. (b) Eighth cable.

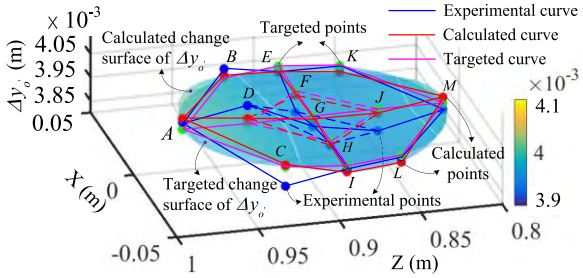

FIGURE 20. Comparison curves between calculated, experimental, and targeted $\Delta y_{O'}$.

experimental cable tension values for controlling TCPR-8 are obtained, as shown in Fig. 19. The pose change values (Δy_A, $\Delta y_B, \ldots, \Delta y_G, \ldots, \Delta y_L$, and Δy_M) in the y direction are recorded by utilizing the laser tracker under the control of the 13 sets of cable tension. The calculated, experimental, and targeted values (the targeted pose change value is 3.9706 in the y direction) of pose change are compared, as presented in Fig. 20 and Table 11.

Similar methods can be used to verify the CSS in the remaining directions. Note: As shown in (3), as gravity is a part of the external force acting on the end-effector, it is necessary to apply a load of $F+$ 20 N (the mass of the end-effector is 2 kg, as shown in Table 2) in the z direction to ensure that the external load, W, is constant in the z direction.

The calculated and experimental curves for $\Delta x_{O'}$ and $\Delta y_{O'}$ have good coherence to the targeted curves, as shown

TABLE 11. Comparison of calculated, experimental, and targeted values of pose change in y direction (in millimeters).

Position	Pose change			
	Calculated	Relative error	Experimental	Relative error
A	4.017	1.17%	4.001	0.77%
B	3.978	0.17%	4.01	0.99%
C	3.980	0.24%	3.888	2.08%
D	3.988	0.44%	4.046	1.90%
E	3.948	0.57%	3.945	0.64%
F	3.955	0.39%	3.884	2.18%
G	3.958	0.32%	3.929	1.05%
H	3.955	0.39%	3.959	0.29%
I	3.948	0.57%	3.96	0.27%
J	3.955	0.39%	3.883	2.21%
K	3.943	0.70%	3.969	0.04%
L	3.943	0.70%	3.963	0.19%
M	3.998	0.70%	3.946	0.62%

in Figs. 18 and 20, respectively. Considering the results provided in Tables 10 and 11, it is clear that the maximum relative errors between the calculated and targeted values of $\Delta x_{O'}$ and $\Delta y_{O'}$ are 2.27% and 1.17%, respectively, and the maximum relative errors between the experimental and targeted values of $\Delta x_{O'}$ and $\Delta y_{O'}$ are 3.60% and 2.21%, respectively. These values meet the engineering requirement of less than 5% error. These results verify that the proposed concepts and methods are correct and effective.

V. CONCLUSION

The concept of the CSS of CDPRs is introduced and defined based on the CTFR, and its calculation method is presented. Considering two constant stiffness planes of a 2-DOR CDPR as an example for calculation and analysis, it is found that the maximum relative errors between the calculated and targeted values are 2.27% and 1.17%, respectively. These values meet the requirement of ground simulation spacecraft landing addressing experiments, which require a constant stiffness working plane with a stiffness error of less than 5%.

Then, an evaluation method for the local and global stability of the CSS is proposed. The method is used to evaluate and analyze the quality of the CSS of the CDPR. Next, the influences of the load and posture of the end-effector of the CDPR on its CSS are analyzed, and the following results are obtained:

(1) As the load increases, the volume of the CSS of the CDPR decreases gradually until it becomes zero and its stability gradually deteriorates.

(2) It is worth noting that as the load in the z and α directions increases, the volume of the CSS of the CDPR first increases and then decreases. In addition, as the load in the z direction increases, the stability of the CSS first improves and then deteriorates.

(3) As the angular displacement of the end-effector's posture increases, the volume of the CSS of the CDPR decreases gradually until it becomes zero, and the stability of the CSS gradually deteriorates.

(4) Similar to the results for the load, as the angular displacement in the β and γ directions increases, the volume of the CSS of the CDPR first increases and then decreases.

(5) The stability of the CSS gradually deteriorates from the center to the edge.

The above analysis results indicate that to ensure the stability of robots in practical applications, the center area of the CSS that is located away from the boundary should be selected as a priority. The volume and stability of the CSS of CDPRs can be improved by increasing the load or angular displacement of the end-effector's posture within a certain range. Additionally, it is necessary to avoid the robot working with a large load and large angular displacement of the end-effector's posture as much as possible.

Finally, two planes (a rectangle and an ellipse) are selected in the CSS of TCPR-8 for experimental verification. The results indicate that in the constant stiffness planes, the maximum relative errors between the experimental and targeted values of $\Delta x_{O'}$ and $\Delta y_{O'}$ are 3.60% and 2.21%. These values meet the engineering requirement that stiffness error must be less than 5%. These results verify that the proposed concepts and methods are correct and effective.

In future research, we will focus on how to quickly determine the appropriate working area in the CSS according to application requirements.

This study considers a 2-DOR CDPR as an example for analysis and experimental verification. Even though such CDPRs are widely used, they do not encompass all possible CDPR designs. Nevertheless, our findings can serve as a reference for analyzing the CSS of other types of redundant CDPRs.

REFERENCES

[1] A. Berti, J.-P. Merlet, and M. Carricato, "Solving the direct geometrico-static problem of underconstrained cable-driven parallel robots by interval analysis," *Int. J. Robot. Res.*, vol. 35, no. 6, pp. 723–739, 2016.
[2] X. Tang, L. Tang, J. Wang, and D. Sun, "Workspace quality analysis and application for a completely restrained 3-Dof planar cable-driven parallel manipulator," *J. Mech. Sci. Technol.*, vol. 27, no. 8, pp. 2391–2399, 2013.
[3] M. Carricato and J.-P. Merlet, "Stability analysis of underconstrained cable-driven parallel robots," *IEEE Trans. Robot.*, vol. 29, no. 1, pp. 288–296, Feb. 2013.
[4] S. H. Yeo, G. Yang, and W. B. Lim, "Design and analysis of cable-driven manipulators with variable stiffness," *Mechanism Mach. Theory*, vol. 69, pp. 230–244, Nov. 2013.
[5] R. Yao, X. Tang, J. Wang, and P. Huang, "Dimensional optimization design of the four-cable-driven parallel manipulator in fast," *IEEE/ASME Trans. Mechatronics*, vol. 15, no. 6, pp. 932–941, Dec. 2010.
[6] P. Dion-Gauvin and C. Gosselin, "Dynamic point-to-point trajectory planning of a three-DOF cable-suspended mechanism using the hypocycloid curve," *IEEE/ASME Trans. Mechatronics*, vol. 23, no. 4, pp. 1964–1972, Aug. 2018.
[7] D. Song, L. Zhang, and F. Xue, "Configuration optimization and a tension distribution algorithm for cable-driven parallel robots," *IEEE Access*, vol. 6, pp. 33928–33940, 2018.
[8] Z. Cui, X. Tang, S. Hou, and H. Sun, "Research on controllable stiffness of redundant cable-driven parallel robots," *IEEE/ASME Trans. Mechatronics*, vol. 23, no. 5, pp. 2390–2401, Oct. 2018.

[9] Y. Hu, L. Tao, J. Jia, and W. Lv, "Control and simulation of cable-driven parallel robots in offshore cargo handling," in *Proc. 11th World Congr. Intell. Control Automat.*, Jun./Jul. 2014, pp. 2451–2455.

[10] J. Albus, R. Bostelman, and N. Dagalakis, "The NIST robocrane," *J. Feild Robot.*, vol. 10, no. 5, pp. 709–724, 1993.

[11] X. J. Jin, D. I. Jun, X. Jin, J. Seon, A. Pott, S. Park, J.-O. Park, and S. Y. Ko, "Upper limb rehabilitation using a planar cable-driven parallel robot with various rehabilitation strategies," in *Cable-Driven Parallel Robots*. Cham, Switzerland: Springer, 2015, pp. 307–321.

[12] G. Rosati, R. Secoli, D. Zanotto, A. Rossi, and G. Boschetti, "Planar robotic systems for upper-limb post-stroke rehabilitation," in *Proc. ASME Int. Mech. Eng. Congr. Expo. (IMECE)*, vol. 2, 2008, pp. 115–124.

[13] Y. Mao, X. Jin, G. G. Dutta, J. P. Scholz, and S. K. Agrawal, "Human movement training with a cable driven ARm EXoskeleton (CAREX)," *IEEE Trans. Neural Syst. Rehabil. Eng.*, vol. 23, no. 1, pp. 84–92, Jan. 2015.

[14] Y. Wang, J. Chen, K. Zhu, B. Chen, and H. Wu, "Practical tracking control of cable-driven robots using adaptive nonsingular fast terminal sliding mode," *IEEE Access*, vol. 6, pp. 68057–68069, 2018.

[15] X. Cui, W. Chen, X. Jin, and S. K. Agrawal, "Design of a 7-DOF cable-driven arm exoskeleton (CAREX-7) and a controller for dexterous motion training or assistance," *IEEE/ASME Trans. Mechatronics*, vol. 22, no. 1, pp. 161–172, Feb. 2017.

[16] X. Jiang and C. Gosselin, "Trajectory generation for three-degree-of-freedom cable-suspended parallel robots based on analytical integration of the dynamic equations," *J. Mech. Robot.*, vol. 8, no. 4, 2016, Art. no. 041001.

[17] S. Tadokoro, Y. Murao, M. Hiller, R. Murata, H. Kohkawa, and T. Matsushima, "A motion base with 6-DOF by parallel cable drive architecture," *IEEE/ASME Trans. Mechatronics*, vol. 7, no. 2, pp. 115–123, Jun. 2002.

[18] J.-A. Seon, S. Park, S. Y. Ko, and J.-O. Park, "Cable configuration analysis to increase the rotational range of suspended 6-DOF cable driven parallel robots," in *Proc. 16th Int. Conf. Control, Automat. Syst. (ICCAS)*, Oct. 2016, pp. 1047–1052.

[19] A. Nasr and S. A. A. Moosavian, "Multi-criteria design of 6-dof fully-constrained cable driven redundant parallel manipulator," in *Proc. 3rd RSI Int. Conf. Robot. Mechatron. (ICROM)*, 2015, pp. 1–6.

[20] R. Chellal, E. Laroche, and L. Cuvillon, "An H∞ methodology for position control of 6-DoF cable-driven parallel robots," in *Proc. Eur. Control Conf. (ECC)*, 2014, pp. 358–363.

[21] H. Jamshidifar, A. Khajepour, B. Fidan, and M. Rushton, "Kinematically-constrained redundant cable-driven parallel robots: Modeling, redundancy analysis, and stiffness optimization," *IEEE/ASME Trans. Mechatronics*, vol. 22, no. 2, pp. 921–930, Apr. 2017.

[22] L. H. Z. Wenba, "Static stiffness analysis of flexible-cable-driven parallel mechanism," *J. Mech. Eng.*, vol. 46, no. 3, pp. 8–16, 2010.

[23] M. Gouttefarde and C. M. Gosselin, "Analysis of the wrench-closure workspace of planar parallel cable-driven mechanisms," *IEEE Trans. Robot.*, vol. 22, no. 3, pp. 434–445, Jun. 2006.

[24] D. Lau, D. Oetomo, and S. K. Halgamuge, "Wrench-closure workspace generation for cable driven parallel manipulators using a hybrid analytical-numerical approach," *J. Mech. Des.*, vol. 133, no. 7, 2011, Art. no. 071004.

[25] C. B. Pham, S. H. Yeo, G. Yang, M. S. Kurbanhusen, and I.-M. Chen, "Force-closure workspace analysis of cable-driven parallel mechanisms," *Mechanism Mach. Theory*, vol. 41, no. 1, pp. 53–69, 2006.

[26] X. Liu, "Analysis on the static stiffness of wire-driven parallel manipulators," *J. Mech. Eng.*, vol. 47, no. 13, pp. 35–43, 2011.

ZHIWEI CUI received the master's degree from Beihang University, Beijing, China, in 2016. He is currently pursuing the Ph.D. degree in mechanical engineering with Tsinghua University, Beijing, China. His research interests include the parallel manipulators, and Cable-Driven Robots.

XIAOQIANG TANG received the Ph.D. degree in mechanical engineering from Tsinghua University, Beijing, in 2001. He is currently a Professor in the Department of Mechanical Engineering, Tsinghua University. His research interests include parallel manipulators, robots, and reconfigurable manufacturing technology.

SENHAO HOU received the B.S. degree from the Beijing Institute of Technology, Beijing, China, in 2016. He is currently pursuing the Ph.D. degree in mechanical engineering with Tsinghua University, Beijing, China. His current research interest include cable parallel robot.

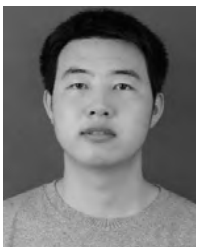

HAINING SUN received the B.S. degree from Shandong University, Jinan, China, in 2017. He is currently pursuing the Ph.D. degree in mechanical engineering with Tsinghua University, Beijing, China. His current research interest include cable parallel robots.

DIANJUN WANG received the Ph.D. degree in control theory and control engineering from Harbin Engineering University, Harbin, in 2004. He is currently a Professor in the Department of Mechanical Engineering, Beijing Institute of Petrochemical Technology. His research interests include mobile robot navigation and location, logistics robot system, and robot integrated manufacturing system.